Morphometrics and machine learning discrimination of the middle Eocene radiolarian species Podocyrtis chalara, Podocyrtis goetheana and their morphological intermediates

Francisco Pinto, Veronica Carlsson, Mathias Meunier, Bert Van Bocxlaer, Hammouda Elbez, Marie Cueille, Pierre Boulet, Taniel Danelian

Morphometrics and machine learning discrimination of the middle Eocene radiolarian species *Podocyrtis chalara*, *Podocyrtis goetheana* and their morphological intermediates

Francisco Pinto[1], Veronica Carlsson[1, 2] *, Mathias Meunier[1], Bert Van Bocxlaer[1], Hammouda Elbez[2], Marie Cueille[1], Pierre Boulet[2] and Taniel Danelian[1]

[1]Univ. Lille, CNRS, UMR 8198, Evo-Eco-Paleo, F-59000 Lille, France.

[2]Univ. Lille, CNRS, CRIStAL – Centre de Recherche en Informatique Signal et Automatique de Lille, UMR 9189, F-59000 Lille, France.

***corresponding author: veronica.carlsson@univ-lille.fr**

Abstract

We present various approaches to distinguish the middle Eocene species *Podocyrtis chalara* and *Podocyrtis goetheana*, which are end members of a trajectory of phenotypic change, and their intermediate morphogroups. We constructed a set of thirteen traditional morphological variables to classify the entire morphological variability encompassed by the two morphospecies and their intermediates *Podocyrtis* sp. cf. *P. chalara* and *Podocyrtis* sp. cf. *P. goetheana*. We used two methods of classification, namely Linear Discriminant Analysis (LDA) and machine learning using artificial neural networks. LDA performed on the morphometric data reveals a good discrimination for *P. chalara*, *P. goetheana* and *Podocyrtis* sp. cf. *P. goetheana*, but not for *Podocyrtis* sp. cf. *P. chalara*. We used three approaches of machine learning based on different neural networks: Convolutional Neural Networks (CNNs) and two Spiking Neural Networks (SNNs). Each of these neural networks was trained based on classified images of the two morphospecies and their morphological intermediates, thus constituting a different set of input data than the morphometric dataset for LDA. The neural network approaches identified the same three morphospecies recognized by LDA from a dataset of traditional measurements, i.e. *P. chalara*, *P. goetheana* and *Podocyrtis* sp. cf. *P. goetheana*, with up to 92 % accuracy. Our results highlight the great potential and promising perspectives of machine learning and neural networks in the application of image-based object recognition for morphological classification, which may also contribute to more objective taxonomic decisions.

Keywords

Morphometrics; Artificial Intelligence; Convolutional Neural Networks; Spiking Neural Networks; Radiolarians; Automated identification

1. Introduction

Polycystine radiolaria are one of the oldest known Rhizarian lineages, with a fossil record stretching back to the Early Cambrian (Obut and Iwata, 2000; Pouille et al., 2011) and is thus of much interest for a number of evolutionary studies (e.g., Danelian and Johnson, 2001, Danelian et al., 2014, Renaudie and Lazarus, 2003, Tetard et al., 2017).

Since the early stages of the Deep Sea Drilling Program, the Cenozoic record of polycystine radiolaria has allowed us to establish their evolutionary and biostratigraphic significance, especially based on representatives of the Eocene genus *Podocyrtis*. (Sanfilippo and Riedel, 1970; Riedel, 1971; Moore, 1972; Riedel and Sanfilippo, 1978). Calibrated initially to the magnetostratigraphic time scale (Sanfilippo and Nigrini, 1998), the middle Eocene tropical radiolarian zones are now tied to orbital chronology (Meunier and Danelian, 20222), which provides the highest resolution of temporal control possible today and allows to define biostratigraphic events more accurately. Indeed, many of the middle Eocene biozones are based on the evolution of the various lineages of the genus *Podocyrtis*, which often relate to gradual anagenetic changes in phenotypes, as documented in several evolutionary lineages since the early 1970s (Sanfilippo and Riedel 1970, 1992; Riedel, 1971). For example, the bases of biozones RP14 and RP15 are defined based on anagenetic phenotypic changes between the morphospecies *P. sinuosa* - *P. mitra* and *P. mitra* - *P. chalara*, respectively.

The *Podocyrtis (Lampterium)* lineage ends with the marked morphological transition of *Podocyrtis chalara* to *P. goetheana*. Interestingly, the first occurrence of *P. goetheana* defines the base of biozone RP16 (Sanfilippo and Nigrini, 1998); an anagenetic transition was reported, but intermediate forms were never documented in detail. The absence of such a documentation has implications for our understanding of evolutionary changes in this *Podocyrtis* lineage, but as intermediate forms are poorly understood it also affects the

recognition of the base of RP16. Here we examine the well-preserved radiolarian material of ODP Sites 1259 and 1260 from Demerara Rise (equatorial Atlantic Ocean), which present an exceptionally expanded Eocene sedimentary sequence. As such, this material offers an exceptional opportunity to study the morphological transitional forms between *P. chalara* and *P. goetheana*.

Within the abovementioned context, the principal aim of our study is to document morphological variation in the anagenetic sequence of *P. chalara* to *P. goetheana* with two different but complementary approaches to test the performance of various machine learning algorithms based on neural networks. To reach this objective, we first quantified morphological variation in the anagenetic transition between *P. chalara* and *P. goetheana* with traditional morphometrics, i.e., linear measurements, pore counts and associated ratios in the framework of qualitatively recognized morphological entities. This quantification of shape follows previous attempts to assess morphological changes in the *Podocyrtis* (*Lampterium*) lineage (Sanfilippo and Riedel, 1990; Rohlf and Bookstein, 1991; Danelian and Macleod, 2019; Watanabe et al., 2022). Using this morphometric framework of measurement data and *a priori* morphospecies assignments, we examined how well linear discriminant analysis allows to distinguish morphospecies as a baseline to test the performance of machine learning with neural networks.

Testing the capabilities of neural network approaches based on image recognition is a daunting task, because during the past couple of years, a variety of techniques involving Artificial Neural Networks (ANNs) have been developed and improved. Convolutional Neural Networks (CNNs) have been specifically designed for analysis of visual data, and are now commonly used for image recognition, warranting detailed examinations of their performance in morphological classification, and, therewith, as a tool to inform, and potentially reach more objective taxonomic decisions. Indeed, CNNs are becoming well-

integrated in various micropaleontological studies for automatic image recognition (i.e., Mitra et al., 2019, Hsiang et al., 2019; Marchant et al., 2020; Dollfus and Beaufort, 1999; Beaufort and Dollfus, 2004; Bourel et al., 2020; Itaki et al., 2020; Renaudie et al., 2018; Tetard et al., 2020). Regarding Eocene radiolaria, a recent study by Carlsson et al. (2022) applied a CNN to eight well-delimited morphospecies of the genus *Podocyrtis*, and documented the potential of this method under the simplified scenario when no morphological intermediates are present. Spiking Neural Networks (SNNs) present another type of neural network, which in addition to neuronal and synaptic states, they also incorporate a time component; this is why such networks can more closely mimic natural neural networks (Maass, 1997). SNNs have wide applicability, including modeling of natural systems such as the central nervous system of biological organisms, as well as for image analysis. Traditionally, SNNs were less accurate than other neural networks, but in recent years their performance has significantly improved; they are more appropriate to process spatio-temporal data, and they may use computational resources more effectively (Tavanaej et al., 2019). As such, an evaluation of SNNs in image recognition and biological classification seems warranted.

In this paper, we expand on previous work by Carlsson et al (2022) with CNNs by aiming to classify stacked and segmented images of the entire spectrum of morphological variation found between *P. chalara* and *P. goetheana*. As mentioned, we used morphometrics to document shape variability, which we subjected together with *a priori* morphospecies assignments to LDA as a baseline to study the classification performance for image-based neural networks using a CNN, a Spike-timing-dependent plasticity (STDP)-based SNN and a SuperSpike-based SNN. This examination allows us to evaluate the use of imaging data and neural networks for automated classification in a complex case study with intermediate shapes. If the neural networks perform well, we would expect correct classification for each morphogroup. Additionally, the results should reflect those of the LDA analysis, if the

morphometric documentation of shape variation is representative of the four morphospecies. Alternatively, neural networks may show differences compared to LDA. These distinctions could arise if neural networks fail to perform well, possibly due to unsuccessful training with the existing data. In opposite to that, the neural networks may perform better than LDA if the data supporting LDA lacks crucial shape information necessary for distinguishing between morphogroups based on the images. As such, we expect our study to shed light into future opportunities for automated biological classification of polycystine radiolaria and the use of neural networks in developing more objective taxonomic decisions.

2. Analyzed morphological groups

Plate 1 displays the entire range of morphological variability observed between *P. chalara* and *P. goetheana*. As linear discriminant analysis and the supervised learning of neural networks are based on *a priori* group assignments, we were required to assign this continuum of variation to a number of morphological groups. Based on extensive qualitative assessments and to challenge the employed classification algorithms we recognized four distinct morphological groups for the purpose of the current study, without currently being concerned by the paleobiological/evolutionary status of each group. These morphogroups are briefly presented below.

Podocyrtis chalara Riedel and Sanfilippo

Pl. 1, fig. A, B

1970 *Podocyrtis* (*Lampterium*) *chalara* Riedel and Sanfilippo, p. 535, pl. 12, figs. 2, 3.

1971 *Podocyrtis* (*Lampterium*) *chalara* Riedel and Sanfilippo: Moore, p. 743, pl. 3, figs. 5, 6.

1972 *Lampterium chalara* Riedel and Sanfilippo: Petrushevskaya and Kozlova, p. 543, pl. 32, fig. 12.

1978 *Podocyrtis* (*Lampterium*) *chalara* (Riedel and Sanfilippo): Riedel and Sanfilippo, p. 71, pl. 8, fig. 3, text-fig. 3.

2012 *Podocyrtis* (*Lampterium*) *chalara* Riedel and Sanfilippo: Kamikuri, p. 103, pl. 3, figs. 2a, 2b.

2012 *Podocyrtis* (*Lampterium*) *chalara* Riedel and Sanfilippo: Moore and Kamikuri, p. 9, pl. P7, fig. 8.

Distinguishing characters: We include here forms displaying twelve or less vertically well-aligned, subangular abdominal pores of similar size per horizontal row, illustrating the classic morphology of *P. chalara*. Specimens of this morphogroup display less than thirteen pores on the circumference of the abdomen.

Podocyrtis sp. cf. *P. chalara* Riedel and Sanfilippo

Pl. 1, fig. C, D

1972 *Lampterium* sp. G: Petrushevskaya and Kozlova, pl. 32, fig. 10.

1972 *Lampterium* sp. aff. *L. goetheana*: Petrushevskaya and Kozlova, pl. 32, fig. 13.

2022 *Podocyrtis* (*Lampterium*) *chalara* Riedel and Sanfilippo: Meunier and Danelian, p. 21, pl. 2.4.

Distinguishing characters: This morphogroup includes specimens that have a similar outline and appearance as *P. chalara*, but they display vertically misaligned subangular abdominal pores of different size. Specimens of this morphogroup may display vertical rows of pores that are shifted to the right or left compared to the rows of pores above and below, giving a

twisted appearance for the rows of pores developed on the abdomen, with result a honeycomb-like pore pattern. These shifts may be so extensive that the arrangement of pores on the abdomen becomes chaotic, preventing the possibility to trace any apparent abdominal rows or vertical alignment.

Podocyrtis sp. cf. *P. goetheana* (Haeckel)

Pl. 1, figs. E - L

2006 *Podocyrtis* (*Lampterium*) *chalara* Riedel and Sanfilippo: Funakawa et al., p. 29, pl. P9, figs. 11a, 11b.

Distinguishing characters: This morphogroup is mainly characterized by an increase in total size, but with a significant reduction in the number of abdominal pores compared to both variants of *P. chalara*. It differs from *P. goetheana* in that the bars of the second row of abdominal pores are thicker and not always elongated, nor parallel to each other, as the formation of the honeycomb-like pattern of pores becomes more apparent. This morphogroup displays a high degree of morphological variability.

Podocyrtis goetheana (Haeckel)

Pl. 1, figs. M - O

1887 *Cycladophora goetheana* Haeckel, p. 1376, pl. 65, fig. 5.

1970 *Podocyrtis* (*Lampterium*) *goetheana* (Haeckel): Riedel and Sanfilippo, p. 535.

1971 *Podocyrtis* (*Lampterium*) *goetheana* (Haeckel): Moore, p. 743, pl. 3, figs. 7, 8.

1972 *Lampterium* sp. aff. *L. goetheana* Petrushevskaya and Kozlova, pl. 32, fig. 14.

2005 *Podocyrtis* (*Lampterium*) *goetheana* (Haeckel): Nigrini et al., p. 45, pl. P5, figs. 11, 12.

2006 *Podocyrtis* (*Lampterium*) *goetheana* (Haeckel): Funakawa et al., p. 29, pl. P9, figs. 12a, 12b.

2012 *Podocyrtis* (*Lampterium*) *goetheana* (Haeckel): Kamikuri, p. 103, pl. 3, fig. 1.

2012 *Podocyrtis* (*Lampterium*) *goetheana* (Haeckel): Moore and Kamikuri, p. 9, pl. P7, fig. 9.

2022 *Podocyrtis* (*Lampterium*) *goetheana* (Haeckel): Meunier and Danelian, p. 21, pl. 2.5.

Distinguishing characters: This group includes only forms that display elongated straight bars formed at the level of the second horizontal row of pores on the abdomen. This feature is typical for *P. goetheana* as originally described, and, as mentioned above, the first occurrence of typical *P. goetheana* defines the base of the RP16 Zone.

Plate 1. Composite light micrographs of *Podocyrtis* radiolaria from ODP Site 1260, processed and scaled in ImageJ. (**A**) and (**B**) *Podocyrtis chalara*, samples: ODP 1260A-6R-5W, 63-65 cm and ODP 1260A-6R-5W, 20-22 cm; (**C**) and (**D**) *Podocyrtis* sp. cf. *P. chalara*, samples: ODP 1260A-6R-4W, 68-70 cm and ODP 1260A-6R-5W, 20-22 cm; (**E**) to (**L**) *Podocyrtis* sp. cf. *P. goetheana*, samples: ODP 1260A-6R-4W, 68-70 cm; ODP 1260A-6R-5W, 15-17 cm and ODP 1260A-6R-5W, 87-89 cm; (**M**) to (**O**) *Podocyrtis goetheana*, sample: ODP 1260A-6R-1W, 58-60 cm.

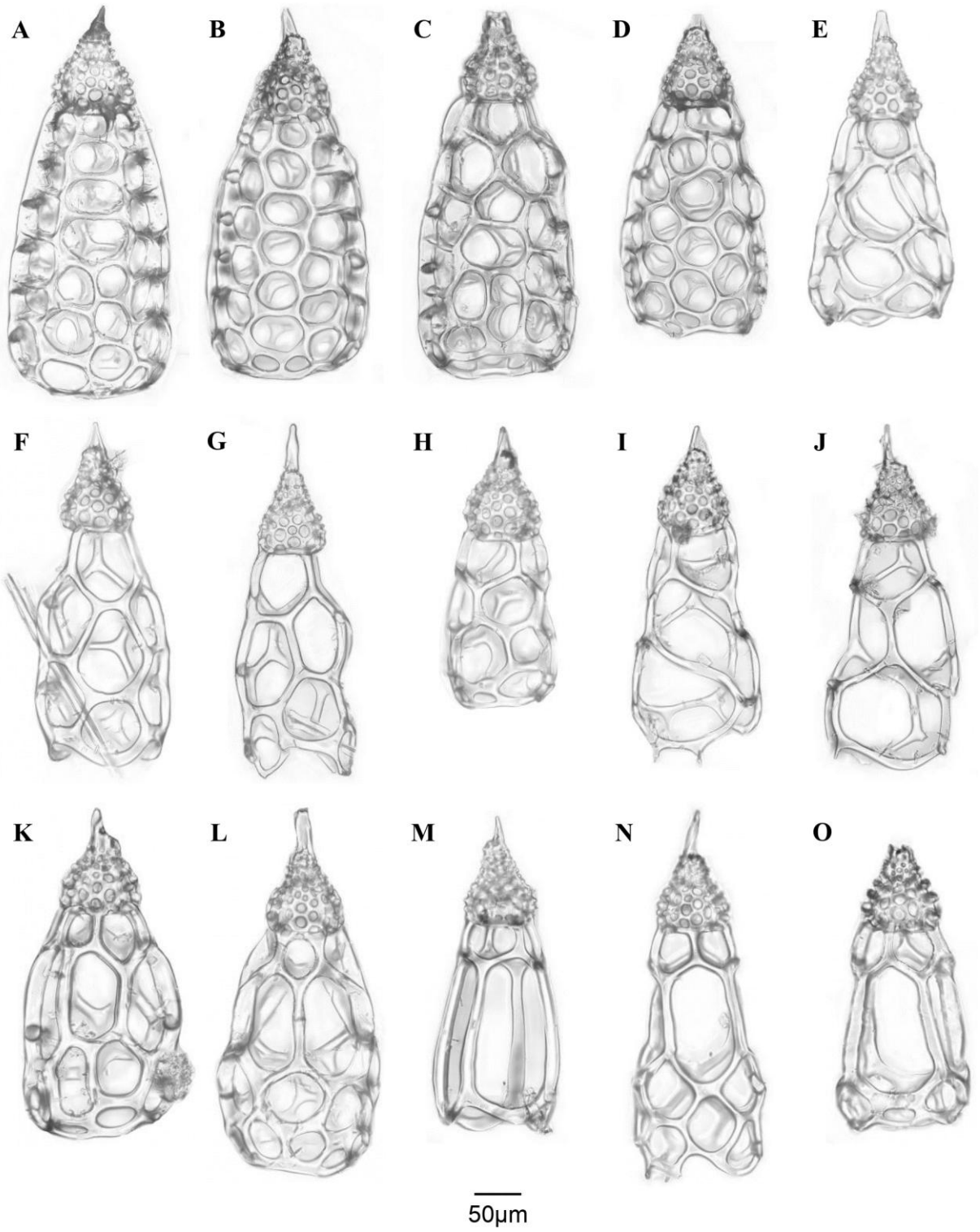

213

214

3. Materials and methods

3.1. Sediment samples

The material analyzed in this study consists of radiolaria obtained from an expanded middle Eocene siliceous chalk sequence drilled at ODP Sites 1259 and 1260 (Leg 207, Demerara Rise), located in the equatorial region of the Atlantic Ocean, 380 km offshore Suriname (Erbacher et al., 2004; Danelian et al., 2005). The middle Eocene sequence is particularly thick at Sites 1259 and 1260 and contains siliceous microfossils (radiolarians, diatoms) of an excellent state of preservation (Danelian et al., 2007; Renaudie et al., 2010; Meunier and Danelian, 2022, 2023). The part of the limestone sequence from Site 1260 that is studied here is dated by orbito-chronology (Westerhold and Röhl, 2013). More specifically, our samples span the interval between 41.24 Ma and 39.84 Ma. Site 1259 is dated via bio- and magneto-stratigraphy and was sampled in the interval between ~39.05 and 37.70 Ma.

3.2. Slide preparation

A combined total of 15 samples from both sites were chosen and prepared for microscopic observation using techniques described by Sanfilippo et al. (1985). A small quantity (~2 cm^3) of unprocessed sediment was collected from each sample and dried overnight at 50°C to eliminate any residual water. After being weighed, sediment samples were soaked for 2 hours in a 500 mL polypropylene beaker containing 30 mL of 30 % hydrochloric acid (HCl), to dissolve their carbonate content and concentrate siliceous microfossils. A few mL of HCl were added at the end to confirm the end of the reaction. The residues resulting from the acid treatment was then washed by adding ~200 mL of distilled water. After 2 hours of decantation, excess water was carefully removed using a pipette. Residues were subsequently soaked for 2 hours in 30 mL of 10 % hydrogen peroxide (H_2O_2)

to remove organic matter, and subsequently washed through a 63 µm sieve using distilled water. The > 63 µm fraction was then exposed to ultrasonic waves for 10 min, then passed again through the 63 µm sieve, and finally left to dry overnight at 50°C. For each sample, ~2 g of dried residue was carefully spread on top of a slide covered with several drops of Norland Optical Adhesive 61, then topped with a coverslip and sealed by two minutes of exposure to UV light.

3.3. Microscopy and image processing

The resulting slides were analyzed with a Zeiss AXIO Images A2 microscope under transmitted light at ×10 and ×20 magnifications. All specimens recognized qualitatively as *P. chalara*, *Podocyrtis* sp. cf. *P. chalara*, *Podocyrtis* sp. cf. *P. goetheana* or *P. goetheana* were manually photographed using the mounted Axiocam ERc5s with Zen 3.5 (blue edition) software. For each specimen, a batch of 5-10 photographs were taken at different focal points to obtain a series of images, which were stacked afterwards using Helicon Focus 7.7.0 (HeliconSoft) to create a composite picture entirely in focus. The stacked images were subsequently retouched with Paint3D to facilitate their automated segmentation. This last procedure was performed with the ImageJ BioVoxxel plugin (Brocher, 2022) and the AutoRadio_Segmenter plugin developed for ImageJ / Fiji (Tetard et al., 2020).

3.4. Morphometric analyses

As we aimed to subject specimens to discriminant analysis based on morphometric measurements, it was essential that the documented morphological variables would adequately capture shape variations present in between the four morphogroups. We first designed a set of variables that would allow to compare with the variables used by Watanabe

et al. (2022) on the specimens of the *Lampterium* lineage from the Pacific Ocean. A subset of seven of these variables was retained and supplemented with six newly proposed variables to result in a set of thirteen morphological variables that document well the morphological variation between the four morphogroups (Figure 1). The seven morphological variables proposed by Watanabe et al. (2022) are:

- W1: Maximal width of the cephalis
- W2: Maximal width of the thorax
- W3: Maximal width of the abdomen
- H1: Maximal height of the cephalis
- H2: Maximal height of the thorax
- H3: Maximal height of the abdomen
- TL: Total length or height of the specimen

and our six additional variables are:

- LP2: Maximum length of the second abdominal pore along along the axis used to measure H3 (with the first pore being the one closest to the thorax-abdomen border)
- NPV: Number of abdominal pores aligned vertically along the axis used to measure H3 (on the front-facing side of the skeleton)
- NPH: Number of abdominal pores aligned horizontally behind the axis of W3 (on the front-facing side of the skeleton)
- R1: Maximum length of the second pore of the abdomen / H3
- R2: Number of abdominal pores aligned vertically behind the axis of H3 / H3
- R3: Number of abdominal pores aligned horizontally behind the axis of W3 / W3

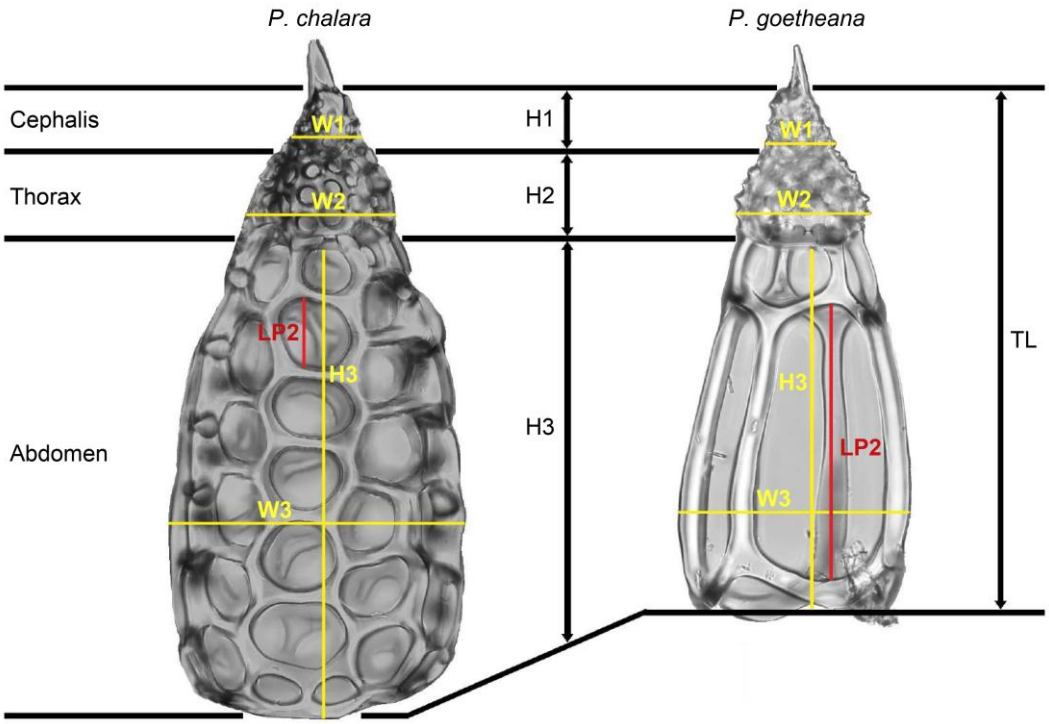

286

287 **Figure 1**. Schematic representation of the eight skeletal variables measured for all specimens outlined in Table
288 1. Five additional variables related to pore counts and ratios are not illustrated. Abbreviations: W1: maximum
289 width of the cephalis; W2: maximum width of the thorax; W3: maximum width of the abdomen; H1: maximum
290 height of the cephalis without the apical horn; H2: maximum height of the thorax; H3: maximum height of the
291 abdomen; TL: total length or height of the specimen without the apical horn; LP2: maximum length of the
292 second abdominal pore.

293

294 Quantifications of these variables (**Table S1** in **Supplementary materials**) were directly
295 performed on a dataset of 214 photographs/specimens from samples 1260A-6R-1W, 58-60
296 cm, 1260A-6R-4W, 68-70 cm, 1260A-6R-5W, 15-17 cm and 1260A-6R-5W, 87-89 cm,
297 outlined in **Table 1**, using the image processing and analysis software ImageJ (Schneider et
298 al., 2012). All of these data were tabulated and then imported in the statistical environment R
299 (v. 4.1.3; R Core Team 2022) for subsequent LDA using the packages MASS (v. 7.3-60;
300 Ripley et al., 2013) and vegan (v. 2.6-4; Oksanen et al., 2013). This analysis is a constrained

ordination procedure that uses a linear combination of coefficients to maximize the distance between *a priori* defined groups, while minimizing the distance within each group (Venables and Ripley, 2002). As morphometric variables were expressed in both metric units and as ratios, the LDA was performed on data that were transformed to have the mean at zero- and one-unit standard deviation (z transformation). After subjecting the whole dataset to LDA we performed cross-validation by 100 replicates of randomly assigning 80 % of the data to a training dataset and the remainder to a testing set to evaluate the classification success of the LDA.

Table 1. Number of specimens analyzed per morphogroup and per sampled core interval.

Samples	*P. chalara*	*Podocyrtis* sp. cf. *P. chalara*	*Podocyrtis* sp. cf. *P. goetheana*	*P. goetheana*	Total number of measured specimens per sample
1260A 6R 1W 58-60cm	0	0	2	29	31
1260A 6R 4W 68-70cm	18	19	37	0	74
1260A 6R 5W 15-17cm	19	12	7	0	38
1260A 6R 5W 87-89 cm	34	9	28	0	71

3.55. Artificial Neural Networks

Artificial Neural Networks or simply neural networks are machine learning algorithms designed to simulate the decision-making processes of the human brain by analyzing and exploiting patterns in data (Yang and Yang, 2014). Prior to analysis, the data given to a network is split into two parts, one for training and one for testing, usually in a 80 to 20 ratio. The first set of data is used to train the neural network, so that to enable it to learn recognizing

features and patterns present in the data, whereas the second set of data is used to test the performance of the network to classify cases based on the previously trained capabilities of recognition.

A type of ANNs that has been specifically designed to analyze visual data are CNNs, commonly used for image recognition. They are designed to analyze visual data by considering the color values of each pixel and by identifying patterns within images (Hijazi et al., 2015). CNNs utilize a process known as convolution. Convolution can be described as a linear operation to decompose the input image by sliding small windows known as filters or kernels over the input image to construct layers that each obtain certain features. The convolutional layers in a CNN modify gradually the image parameters, such as weights or bias, to learn and recognize specific patterns or objects in the images. By adjusting these parameters through training, the network aims to correctly classify the output given a particular input. When a CNN has multiple layers, typically more than three, the procedure is referred to as deep learning, as each layer enables the recognition of more and more advanced features in an image. As mentioned, SNNs consider additionally the time factor, alike biological neurons, which use discrete spikes to compute and transmit information, instead of characterizing neurons by a single, static continuous-valued activation.

The hyperparameters (i.e. weights) of the neural network analyzed in this study were chosen randomly; more specifically a value between -1 and 1 was chosen for the VGG16 and SuperSpike-based networks, while a value network between 0 and 1 was chosen for the STDP-based network neural. We analyzed two sets of stacked and segmented images. The first set contained images with *a priori* assignments to the four morphogroups represented in section 2; for the second set assignments were altered based on the results of LDA. In each case, we performed ten runs per type of neural network used, with 20 epochs for each network, except for the STDP-based network that was run with 100 epochs. An epoch simply

means how many passes it goes through the training set and updates parameters based on each pass. The following neural networks were used to perform runs:

- Visual Geometry Group 16 (VGG16). This 16-layer deep CNN was used for its simplicity. For our analyses, we use transfer learning, meaning that the first 15 layers were already pre-trained based on a large-scale image dataset from ImageNet, and we only trained the last layer specifically using our data and PyTorch (Paszke et al., 2019). More information about VGG16 is provided by Simonyan and Zisserman (2015).
- STDP-based Spiking Neural Network (STDP-Network). This network contains convolutional and pooling layers that learn the features from the data using a Spike Timing Dependent Plasticity (STDP), a learning algorithm inspired by natural neurons. STDP adapts the synaptic connections between the neurons based on the timing of the spikes to transmit information (Masquelier and Thorpe, 2007) in an unsupervised way, i.e., without *a priori* group assignments. This SNN is then combined with a Support Vector Machine (SVM) for classification in the STDP-based network using the *a priori* group assignments (Cortes and Vapnik, 1995). To train the STDP-Network, we used the CSNN-simulator (Falez, 2019).
- SuperSpike-based Spiking Neural Network (SuperSpike-Network). This SNN is trained using a nonlinear voltage-based three-factor learning rule capable of training multilayer networks called the SuperSpike (Zenke and Ganguli, 2018), which is a supervised global learning rule similar to deep learning. We used the Norse simulator for our analyses (Pehle and Pedersen, 2021).

All the neural network simulations were conducted on the cluster “grouille” of the Grid’5000 test bed (Balouek et al., 2013) using two Nvidia A100-PCIE-40GB GPUs, an AMD EPYC

7452 32 core CPU (Zen 2, 2 CPUs/node), and 128GB of RAM. For each type of neural network, we averaged the assignment accuracies obtained over the ten replicate runs to gain robust insight into performance.

The training of the neural networks are expected to be better when a large, data-rich training set is used. Because our two analyzed datasets (Tables 2 and 3) are composed of 428 and 514 original images, respectively, we considered it necessary to augment the data available for ANN training. Therefore, we performed the following data augmentation procedures:

- Rotate the images by a randomized angle between -15 and 15 degrees and keep all copies.
- Randomly choose images that would be flipped from left to right and keep both copies.
- Rescale random images with values between 1 and 1.3 (with 1 being the default scale value).

The total number of images in each dataset was enhanced to >1000 images via data augmentation.

Table 2. List of images included (prior to augmentation) in each of the classes for the four- class dataset used for analysis withVGG16with.

Samples	*P. chalara*	*Podocyrtis* sp. cf. *P. chalara*	*Podocyrtis* sp. cf. *P. goetheana*	*P. goetheana*	Total number of analyzed specimens per sample
1260A 6R 4W 68-70cm	0	19	34	3	56
1260A 6R 4W 119-121cm	0	13	2	1	16
1260A 6R 5W 15-17cm	0	12	7	0	19
1260A 6R 5W 63-65cm	22	9	15	0	46
1260A 6R 5W 87-89 cm	33	12	18	14	77
1260A 6R 6W 20-22 cm	12	18	9	0	39
1260A 6R 6W 57-59 cm	19	14	2	0	35
1260A 7R 1W 22-24 cm	24	15	0	0	39
1260A 7R 1W 69-71 cm	33	11	0	0	44

1260A 7R 1W 121-123 cm	31	11	0	0	42
1260A 7R 2W 19-21 cm	0	13	0	0	13
1260A 8R 3W 65-67cm	0	1	0	0	1
TOTAL	**174**	**148**	**87**	**18**	**427**

Table 3. List of images included (prior to augmentation) in each of the classes for the three class three dataset used for analysis with VGG16, STDP- based SNN and SuperSpike-based SNN.

Samples	***P. chalara* + *Podocyrtis* sp. cf. *P. chalara***	***Podocyrtis* sp. cf. *P. goetheana***	***P. goetheana***	**Total number of analyzed specimens per sample**
1259A 17R 1W 54-56cm	0	0	1	1
1259A 18R 1W 53-55cm	0	0	41	41
1259A 18R 2W 53-55cm	0	0	36	36
1260A 6R 1W 58-60cm	0	1	26	27
1260A 6R 4W 68-70cm	19	29	0	48
1260A 6R 4W 119-121cm	13	2	1	16
1260A 6R 5W 15-17cm	12	5	0	17
1260A 6R 5W 63-65cm	31	15	0	46
1260A 6R 5W 87-89cm	43	28	0	71
1260A 6R 6W 20-22cm	29	8	0	37
1260A 6R 6W 57-59cm	34	2	0	36
1260A 7R 1W 22-24cm	39	0	0	39
1260A 7R 1W 69-71cm	44	0	0	44
1260A 7R 1W 121-123cm	42	0	0	42
1260A 7R 2W 19-21cm	13	0	0	13
TOTAL	**319**	**90**	**105**	**514**

383

384 ## 4. Results

385 ### 4.1. Morphometrics and linear discriminant analysis

386 The LDA performed on the matrix of our 13 morphometric variables, i.e., measurements, pore
387 counts and ratios, represented >99 % of the variation on the first two axes and clustered
388 *Podocyrtis goetheana* and *Podocyrtis* sp. cf. *P. goetheana* successfully (Fig. 2).
389 Comparatively, specimens belonging to *P. chalara* were regularly confused with *Podocyrtis*

sp. cf. *P. chalara* and *vice versa*, resulting overall in 73.5 ± 6.1 % (mean ± sd) correct assignments (Table 4). These two latter morphogroups overlap completely on the LDA plot, whereas *P. Podocyrtis* sp. cf. *P. goetheana* and *P. goetheana* are relatively well-separated from *P. chalara* and *Podocyrtis* sp. cf. *P. chalara*, although they share limited overlap with each other (Figure 2). The first axis of the LDA mainly represents size variations of the second row of abdominal pores. The morphological variables that contribute the most to discriminate the morphogroups on the first LDA axis correspond to the maximum length of the second abdominal pore (LP2), and the maximum length of the second pore of the abdomen/maximum height of the abdomen (R1).

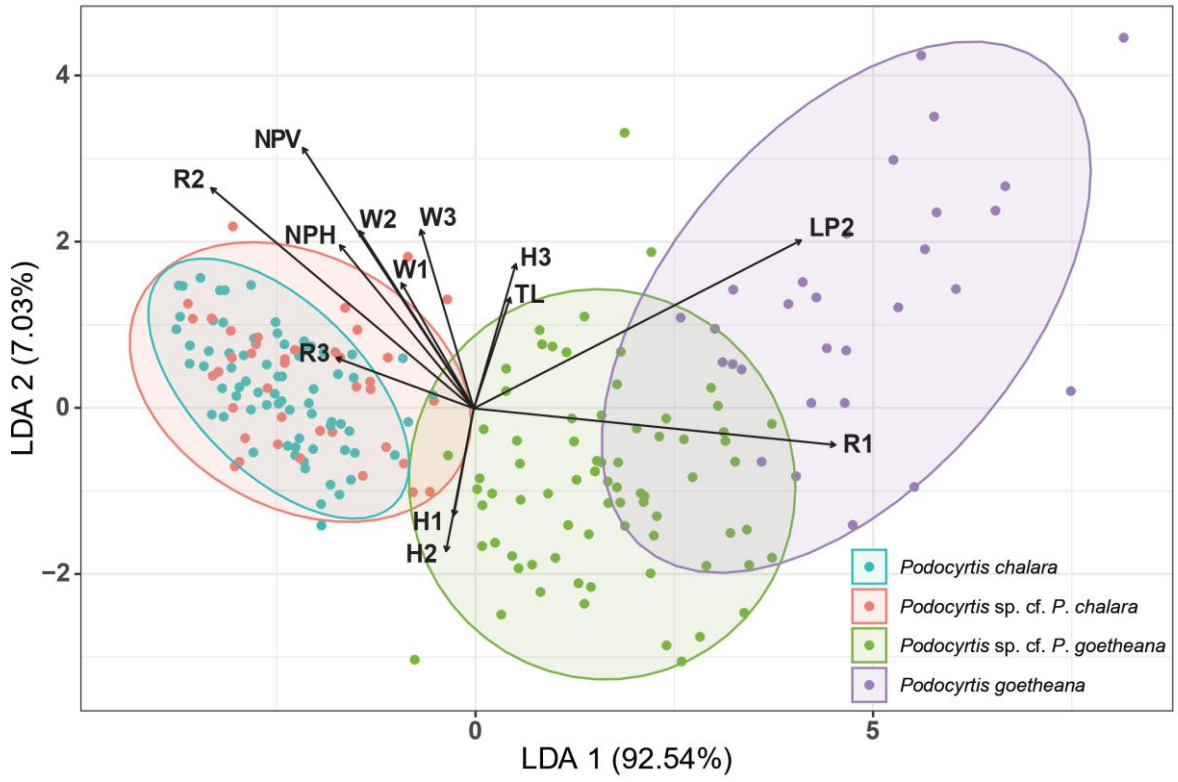

Figure 2. Scatter plot of the two first axes of the Linear Discriminant Analysis (LDA) conducted on the 13 variables that constituted the morphometric data using four *a priori* identified morphogroups (indicated in the legend; ellipses correspond to the 95 % confidence intervals for each morphogroup). Abbreviations: W1: maximum width of the cephalis without the apical horn; W2: maximum width of the thorax; W3: maximum width of the abdomen; H1: maximum height of the cephalis; H2: maximum height of the thorax; H3: maximum height of the abdomen; TL: total length or height of the specimen without the apical horn; LP2: maximum length

406 of the second abdominal pore; NPV: number of abdominal pores aligned vertically; NPH: number of abdominal
407 pores aligned horizontally; R1: maximum length of the second pore of the abdomen/H3; R2: number of
408 abdominal pores aligned vertically/H3; R3: number of abdominal pores aligned horizontally/W3.

409

410 Upon considering three morphogroups achieved by lumping *P. chalara* and *Podocyrtis* sp. cf.
411 *P. chalara*, the LDA ordination is highly similar to that obtained in the four-group analysis,
412 with all variation represented on the first two axes (~92.87 % on axis 1; **Figure S1**).
413 Classification results improved substantially, with 94.5 ± 3.1 % of correctly identified
414 specimens in the three-group LDA (Table S2). Misclassification mainly occurred between *P.*
415 *goetheana* and *Podocyrtis* sp. cf. *P. goetheana*, occasionally also between *P. chalara* and
416 *Podocyrtis* sp. cf. *P. goetheana*, but never between *P. chalara* and *P. goetheana*.

417 **Table 4.** Average confusion matrix of the *Podocyrtis* morphotypes based on linear discriminant analysis (LDA)
418 performed on the matrix of our 13 morphometric variables (.,i.e., measurements, pore counts and ratios).

LDA results 4-group scenario

	P_sp_cf_P_cha_&_P_sp_cf_P_goe	P_cha_&_P_sp_cf_P_cha	P_cha_&_P_sp_cf_P_goe	P_goe_&_P_sp_cf_P_cha	P_goe_&_P_sp_cf_P_goe	P_goe_&_P_cha	total_correct
res_mean	0.011162791	0.204651163	0.001627907	0	0.04744186	0	**0.735116279**
res_sd	0.013819733	0.059589621	0.005963544	0	0.024717954	0	**0.061297375**

419

420

421 ## 4.2. Artificial neural networks

422 ### 4.2.1. Classification using the four morphogroups

423 First, we trained neural networks on the dataset of 428 images attributed to the four
424 morphogroups (**Table 2** 4_classes dataset) using a CNN with a VGG16 architecture. Prior to
425 the training and testing phases, images were manually grouped into four distinct classes (one

class per morphogroup). The analysis was run ten times with the pre-processing parameters outlined in **Table 5**, which resulted to an identification accuracy of 54.4 ± 1.7 % (**Figure 3**).These results indicate that, although the network was able to partially identify the differences between the general morphologies of *P. chalara* + *Podocyrtis* sp. cf. *P. chalara* *versus* those of *P. goetheana* + *Podocyrtis* sp. cf. *P. goetheana*, it was not able to accurately distinguish all four morphogroups from each other.

Table 5. Summary of the tests performed on the 4_classes and 3_classes datasets using VGG16, STDP-based SNN and SuperSpike-based SNN. Accuracy values are averaged from the results of the respective 10 test runs and indicated as the mean ± one standard deviation.

Dataset	Architecture	Test runs	Number of Epochs	Data pre-processing	Simulation time h:m:s	Accuracy (%) ± std mean ± std
4_classes	VGG16	10	20	Image resize to (224, 224) px	0:31:46	54.40 ± 1.74
3_classes	VGG16	10	20	Image resize to (224, 224) px	0:17:37	92.60 ± 0.77
	STDP-Network	10	100	Image resize to (128, 128) px & On-Off filter	0:05:4343	90.40 ± 0.4949
	SuperSpike-Network	10	20	Image resize to (128, 128) px	0:23:26	84.42 ± 1.36

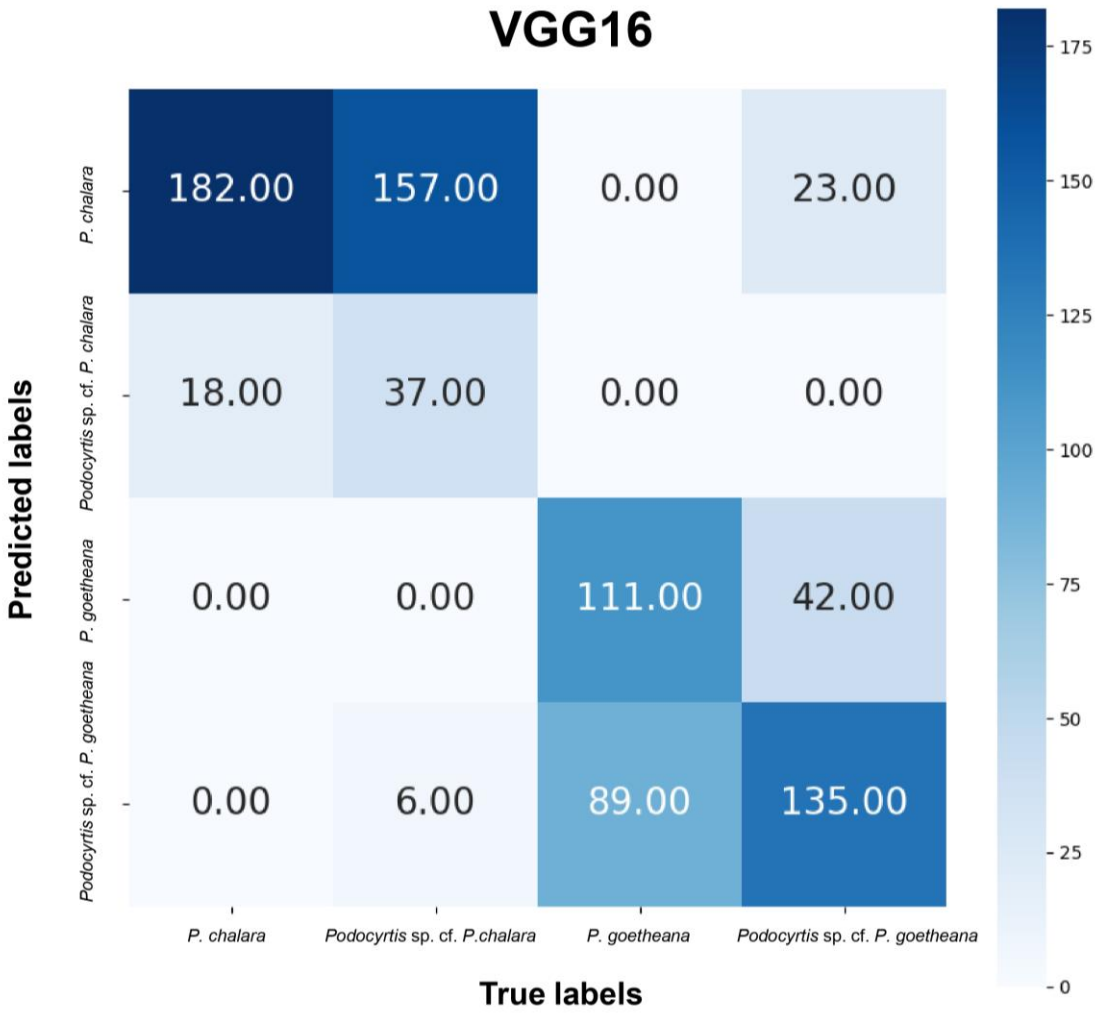

Figure 3. Example of a confusion matrix obtained from random single run – Analysis of 4_classes dataset with VGG16. Correct assignments were reached in 54.40 % of the cases. The color scale indicates the number of specimens.

4.2.2. Classification using the three morphogroups supported by LDA

Subsequently, we trained neural networks using a dataset with *a priori* assignment to the three morphogroups that were recognized by LDA, i.e., *P. chalara* + *Podocyrtis* sp. cf. *P. chalara Podocyrtis* sp. cf. *P. goetheana* and *P. goetheana*. For these analyses we compared the performance of a VGG16 CNN, a STDP-based SNN and a SuperSpike-based SNN using the 3_classes dataset (**Table 3**). The resulting assignment results and average network

accuracies (**Figure 4**) indicate that, under our specified conditions, all neural networks are able to accurately assign specimens to their correct class when three predefined classes are used in combination with a large dataset of images. However, we observed substantial differences in the speed to conclude analyses; thus the STDP-based SNN was the fastest (around 6 minutes) due to the use of the local learning rule for training and one spike per image per neuron principale. Moreover, VGG16 came second with a time of around 17 minutes due to the size of the network and the use of transfer learning and training of only the last layer. Last came the SuperSpike-based SNN with approximately 23 minutes per run because all layers of the network were trained from scratch during the training phase at the start of each run using a global learning rule.

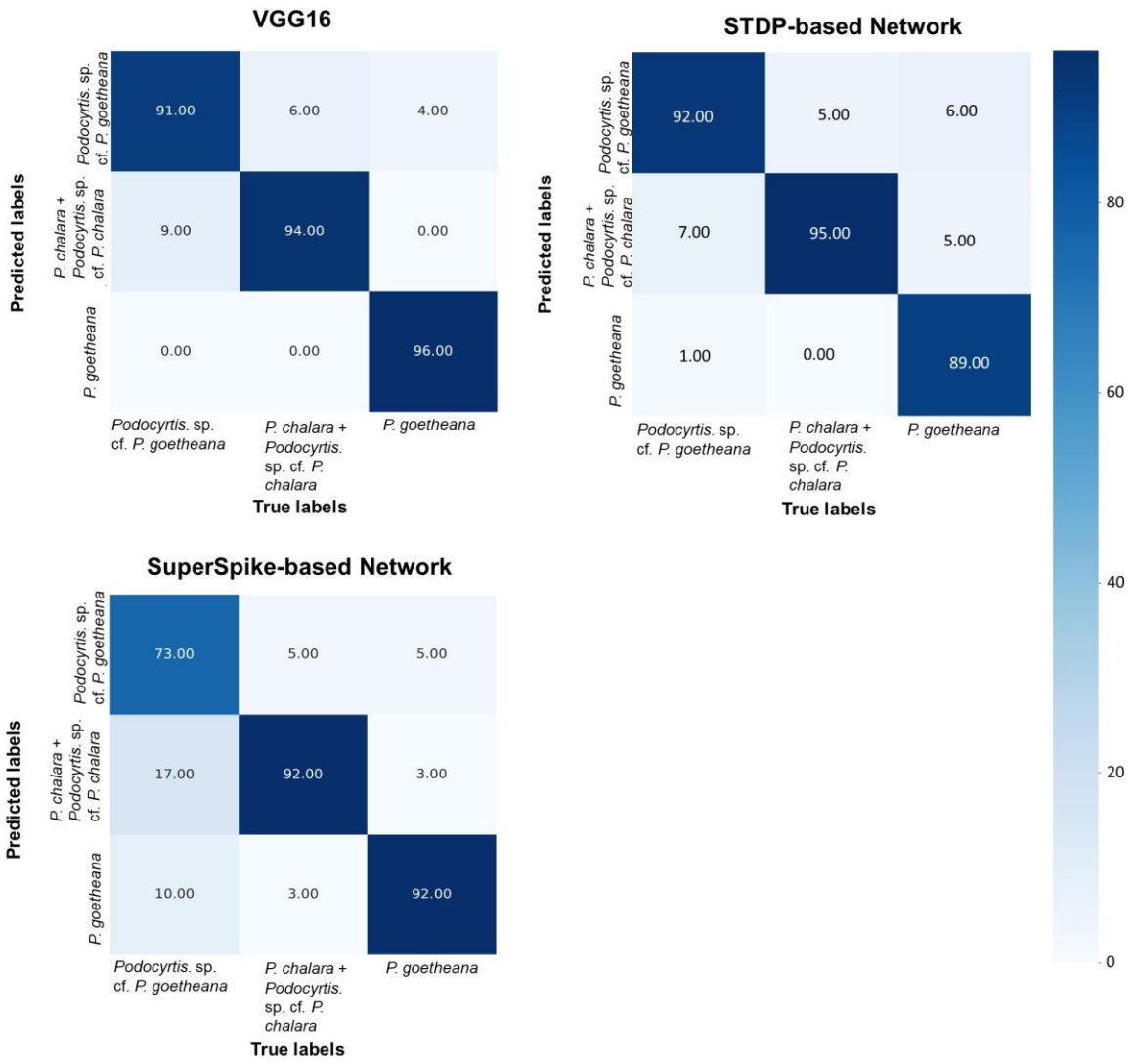

459

460 **Figure 4.** Examples of confusion matrices obtained from random single runs – Analyses of 3_classes dataset
461 with VGG16, STDP-based SNN and SuperSpike-based SNN. Correct assignments were reached in 92.60 %,
462 90.40 % and 84.42 % of the cases in VGG16, STDP-based SNN and SuperSpike-based SNN, respectively. The
463 color scale indicates the number of specimens.

464

465

5. Discussion

In this study, we examined the morphological variability in Eocene *Podocyrtis* belonging to the anagenetic sequence that starts with *P. chalara* and ends with *P. goetheana*. Specifically, we examined and compared the performance of two analytical approaches in assigning individuals to *a priori* defined morphogroups that were constructed from qualitative observations, i.e., *P. chalara*, *Podocyrtis* sp. cf. *P. chalara*, *Podocyrtis* cf. *P. goetheana* and *P. goetheana*. The first approach involved LDA based on morphometric data, whereas the second was a neural network approach based on automatic image recognition. Both methods gave very similar results, which indicates that both morphometrics and image analysis evaluated shape differences in a highly similar way, suggesting that the results obtained with these two different methods are robust.

Comparing LDA and neural network approaches, assignment performances were comparatively low when four morphogroups were considered in the morphological transition from *P. chalara* to *P. goetheana*. The scatterplot of the LDA (**Figure 2**), indicated a large morphospace overlap between *P. chalara* and *Podocyrtis* sp. cf. *P. chalara*, revealing that the qualitatively observed 'differences' were either not sampled in our datasets or that these differences are part of a larger spectrum of morphological variation and not informative to distinguish morphogroups. Given the similarity of LDA and neural networks, based on different datasets, the second hypothesis is more likely; it appears that *P. chalara* and *Podocyrtis* sp. cf. *P. chalara* represent a single highly variable morphogroup. Morphospace overlap is also observed in the LDA between *Podocyrtis* sp. cf. *P. goetheana* and *P. goetheana*, but it is much more limited than between *P. chalara* and *Podocyrtis* sp. cf. *P. chalara*. Finally, *Podocyrtis* sp. cf. *P. goetheana* also overlaps with *P. chalara* and *Podocyrtis* sp. cf. *P. chalara* in morphospace occupation, however this overlap is small. The analyses conducted with the machine learning approach on four morphogroups confirm the results of

LDA, as VGG16 had significant difficulties in differentiating specimens of *P. chalara* from *Podocyrtis* sp. cf. *P. chalara* and *vice-versa* using stacked and segmented images, when all four morphogroup classes were pre-defined. This was also the case for some specimens of *Podocyrtis* sp. cf. *P. goetheana* and *P. goetheana*, which all resulted in an inferior performance of VGG16 compared to that of the LDA for the scenario with four morphogroups,, i.e., 54.4 ± 1.7 % versus 73.5 ± 6.1 %, respectively.

When *P. chalara* and *Podocyrtis* sp. cf. *P. chalara* are lumped in the same morphogroup, resulting in a three-group configuration, assignment probabilities improved strongly both for LDA and neural networks. On average 94.5 ± 3.1 % of assignments were correct with LDA, whereas 92.6 ± 0.8 %, 90.4 ± 0.5 % and 84.4 ± 1.4 % of the assignments were correct for VGG16, STDP-based SNN and SuperSpike-based SNN, respectively. Neural networks, mainly our CNN can accurately and quickly, assign specimens to the three pre-defined classes using a large dataset. Whereas the CNN performed highly similarly to LDA, both SNNs we used here performed less well, as had been documented for other tasks before (Tavanaej et al., 2019). Runs with the STDP-based SNN ran to completion fastest and given that the accuracy was only slightly reduced compared to LDA and VGG16, this approach may be preferred for datasets that require a very long runtime with similar CNNs. The accuracy of the SuperSpike-based SNN was significantly reduced compared to all the other classification methods that we used. Further work is required to determine the cause of this underperformance, but the lower accuracy for the SuperSpikeSuperSpike-based SNN is possibly due to the network size, as we used only using eight layers in our case compared to 16 layers in VGG-16.

As for the performance evaluation of the neural network approach, it is noteworthy that images were obtained manually for the purpose of our study, but advances in image technology now allow that much of the image acquisition and preparation procedures (photographing, stacking and segmentation) to be automated by the use of automatic

516 microscopes and modification of the AutoRadio_Segmenter plugin's code (Marchant et al.,
517 2020; Tetard et al., 2020). Using these automated procedures would facilitate the scalability
518 of the entire analysis with larger datasets. If such automated procedures were to be used,
519 constructing image datasets may potentially become more time-efficient than the various
520 procedures that are required to develop a morphometric dataset. Another advantage of using
521 neural network is their quick run time (**Table 5.**), although both accuracy and run time would
522 increase upon using larger image datasets. Furthermore, standardizing the rotation and
523 orientation of specimens is essential in morphometric studies; however, this requirement can
524 be relaxed for neural networks, as in our case re-rotating and re-orienting were used in the
525 data augmentation process to enlarge input datasets.

526 In our study, we evaluated assignment accuracy of LDA and machine learning with
527 neural networks based on *a priori* group assignments; however, in the future, it would be
528 useful to examine morphological variation without considering such assignments, e.g., by
529 using other ordination techniques and/or by using unsupervised machine learning techniques.
530 These methods could help in attempts to evaluate whether the three retained morphogroups
531 represent natural entities, although based on fossil evidence only such assessments are very
532 difficult. We refrain from such analyses here, as we believe these would be best conducted
533 with a larger set of material that ideally would cover the total geographic range and the total
534 stratigraphic interval covered by *P. chalara*, *Podocyrtis* sp. cf. *P. goetheana* and *P.*
535 *goetheana*.

536 Future work could also be focused on trying to evaluate the capacity of VGG16 to
537 accurately differentiate between the *P. chalara* and *Podocyrtis* sp. cf. *P. chalara* specimens,
538 with an altered set of images. Indeed, the weighted activation heatmap (Grad-CAM)
539 (Servaraju et al., 2017) generated from the runs with the 3-class dataset showed that the
540 analytical focus of the network was centered around the thoracic and abdominal walls of the

541 specimens (**Figure S22** in **Supplementary material**). One could try to develop a dataset
542 including several unstacked and non-segmented images per specimen, each one with a focus
543 on specific morphological features. This would allow some images to contain as much detail
544 as possible on abdominal features, whereas others would focus on other regions (e.g. the
545 thorax) and include blurred features of the outer walls and backside of the abdomen. We
546 hypothesize that these manipulations could force the network to focus its recognition
547 capabilities on a larger set of morphological features. If this hypothesis would be correct, it
548 would also facilitate the data acquisition process by eliminating the need to stack and segment
549 the images themselves. Alternatively, it is possible that providing more fragmented
550 information to neural networks would hamper an efficient learning process, with negative
551 consequences on the accuracy of the following predictions, somewhat similar to what we
552 observed in the VGG16 evaluation based on the 4-class dataset.

553

554 ## 6. Conclusion

555 The aim of our work was to study the morphological variability in the anagenetic sequence of
556 *P. chalara* to *P. goetheana* and to evaluate the performance of recognizing and classifying
557 four *a priori* identified morphogroups with various machine learning algorithms based on
558 neural networks that use image data as direct input in comparison to linear discriminant
559 analysis using morphometric data. Our results demonstrate that LDA and neural networks
560 provide very similar outcomes, indicating robust performances. With both approaches we
561 encountered difficulties distinguishing *P. chalara* and *Podocyrtis* sp. cf. *P. chalara*,
562 suggesting that the qualitative basis on which these morphogroups were recognized is to be
563 revised. For both approaches, assignment probabilities drastically increased for the scenario
564 where three morphogroups were recognized, lumping *P. chalara* and *Podocyrtis* sp. cf. *P.*
565 *chalara*, and thus retaining *P. chalara* + *Podocyrtis* sp. cf. *P. chalara*, *Podocyrtis* sp. cf. *P.*

goetheana and *P. goetheana*. Further studies with more comprehensive sampling are required to document the likelihood of *Podocyrtis* sp. cf. *P. goetheana* representing a separate natural entity, which additionally has implications for the position of bioevent RP16. However, our results indicate that the morphometric data that we used for LDA samples the morphological variability in the anagenetic sequence of *P. chalara* to *P. goetheana* in a comprehensive way. Secondly, neural network approaches were able to correctly assign most specimens, and therewith to accurately distinguish the three morphogroups directly from specimen images. These results indicate that VGG16, STDP-based SNNs, and even SuperSpike-based SNNs are capable of recognizing morphological variation in images and thus of reliably distinguishing radiolarian morphogroups, which could fascilitate identification and help with reaching more objective taxonomic decisions. Furthermore, neural network approaches can be combined with automated image acquisition and preparation procedures (photographing, stacking and segmentation) that enable the creation of much larger image databases in a time-efficient manner. Analyses based on neural network architecture could thus take a fraction of the time that would be required for a trained taxonomist/(paleo)biologist to create and analyze quantitative morphometric datasets. In conclusion, neural network approaches based on images of (paleo)biological specimens may provide promising opportunities to guide more objective taxonomic decisions.

Data availability

Microscopic slides are prepared and stored at UMR 8198 – Evo-Eco-Paleo of the University of Lille, France. The datasets (https://doi.org/10.57745/8KBOFP, Pinto et al. 2023) have been archived in the repository of the University of Lille at Recherche Data Gouv. The codes are available at https://archive.softwareheritage.org/browse/directory/cc7d8ef1505299a208adcde597a98d90b

0ca47d6/https://archive.softwareheritage.org/browse/directory/cc7d8ef1505299a208adcde597a98d90b0ca47d6/ (Elbez, 2023).

Acknowledgments

This study was partly funded by the French government through the program "Investissements d'avenir" (I-ULNE SITE/ANR-16-IDEX-0004 ULNE) managed by the National Research Agency. It also received funding from the European Union's Horizon 2020 research and innovation program under the Marie Sklodowska-Curie grant agreement no. 847568. It was also supported by UMR 8198 Evo-Eco-Paléo and IRCICA (CNRS and Univ. Lille USR-3380).

A special thanks to Mazdak Fatahi for very helpful discussions regarding machine learning techniques and to Sylvie Regnier for help and advice with the sample preparation.

References

Balouek, D., Carpen Amarie, A., Charrier, G., Desprez, F., Jeannot, E., Jeanvoine, E., Lèbre, A., Margery, D., Niclausse, N., Nussbaum, L., Richard, O., Perez, C., Quesnel, F., Rohr, C., & Sarzyniec, L., 2013, Adding virtualization capabilities to the Grid'5000 testbed: In Cloud Computing and Services Science, Communications in Computer and Information Science). Springer International Publishing, v. 367, p. 3-20.

Beaufort, L., and Dollfus, D., 2004, Automatic recognition of coccoliths by dynamical neural networks: Marine Micropaleontology, v. 51, p. 57-73. doi:10.1016/j.marmicro.2003.09.003.

Bourel, B., Marchant, R., de Garidel-Thoron, T., Tetard, M., Barboni, D., Gally, Y., and Beaufort, L., 2020, Automated recognition by multiple convolutional neural networks of modern, fossil, intact and damaged pollen grains: Computers and Geosciences, v. 140, 104498. doi:10.1016/j.cageo.2020.104498.

Brocher, J., 2022, biovoxxel/BioVoxxel-Toolbox: BioVoxxel Toolbox v2.5.3. Zenodo. doi:10.5281/zenodo.5986129.

Carlsson, V., Danelian, T., Boulet, P., Devienne, P., Laforge, A., and Renaudie, J., 2022, Artificial intelligence applied to the classification of eight middle Eocene species of the genus *Podocyrtis* (polycystine radiolaria): Journal of Micropalaeontology, v. 41, p. 165–182.

Cortes, C., and Vapnik, V., 1995, Support-vector networks: Machine Learning, v. 20, p. 273–297.

Danelian, T., and Johnson, K.G., 2001, Patterns of biotic change in Middle Jurassic to Early Cretaceous Tethyan radiolarian: Marine Micropaleontology, v. 43, p. 239-260. doi:10.1016/S0377-8398(01)00029-9.

Danelian, T., and Macleod, N., 2019, Morphometric Analysis of Two Eocene Related Radiolarian Species of the Podocyrtis (Lampterium) Lineage: Paleontological Research, v. 23, p. 314–330.

Danelian, T., Zambetakis-Lekkas, A., Galoyan, G., Sosson, M., Asatryan, G., Hubert, B., and Grigoryan, A., 2014, Reconstructing Upper Cretaceous (Cenomanian) paleoenvironments in Armenia based on Radiolaria and benthic Foraminifera; implications for the geodynamic evolution of the Tethyan realm in the Lesser Caucasus: Palaeogeography, Palaeoclimatology, Palaeoecology, v. 413, p. 123–132.

Danelian, T., Baudin, F., Gardin, S., Masure, E., Ricordel, C., Fili, I., Meçaj, T., and Muska, K., 2007, The record of mid Cretaceous oceanic anoxic events from the Ionian zone of southern Albania: Revue de Micropaléontologie, v. 50, p. 225–237.

Danelian, T., Le Callonec, L., Erbacher, J., Mosher, D.C., Malone, M.J., Berti, D., Bice, K.L., Bostock, H., Brumsack, H.-J., Forster, A., Heidersdorf, F., Henderiks, J., Janecek, T.J., Junium, C., Macleod, K., Meyers, P.A., Mutterlose, J.H., Nishi, H., Norris, R.D., Ogg, J.G., O'Regan, M.A., Rea, B., Sexton, P., Sturt-Fredricks, H., Suganuma, Y., Thurow, J.W., Wilson, P.A., Wise, S.W., and Glatz, C., 2005, Preliminary results on Cretaceous-Tertiary tropical Atlantic pelagic sedimentation (Demerara Rise, ODP Leg 207): Comptes Rendus Geoscience, v. 337, p. 609–616.

Dollfus, D., and Beaufort, L., 1999, Fat neural network for recognition of position-normalized objects. Neural Networks, v.12, p. 553-560. doi:10.1016/S0893-6080(99)00011-8.

[code] Elbez, H., 2023, Code for: Morphometrics and machine learning discrimination of the middle Eocene radiolarian species *Podocyrtis chalara*, *P. goetheana* and their morphological intermediates, deposited at https://archive.softwareheritage.org/browse/directory/cc7d8ef1505299a208adcde597a98d90b0ca47d6/ 2023-08-24.

Haeckel, E., 1887, Report on the Radiolaria collected by H.M.S. Challenger during the years 1873-1876. Report on the Scientific Results of the Voyage of H.M.S. Challenger during the years 1873-1876. 18: 1-1803.

Falez, P., 2019, Improving Spiking Neural Networks Trained with Spike Timing Dependent Plasticity for Image Recognition [phdthesis]: Université de Lille.

Hijazi, S., Kumar, R., and Rowen, C., 2015, Using Convolutional Neural Networks for Image Recognition: Cadence, Cadence Design Systems Inc., p. 1–12.

Hsiang, A.Y., Brombacher, A., Rillo, M.C., Mleneck-Vautravers, M.J., Conn, S., Lordsmith, S., Jentzen, A., Henehan, M.J., Metcalfe, B., Fenton, I.S., Wade, B.S., Fox, L., Meilland, J., Davis, C. V., Baranowski, U., Groeneveld, J., Edgar, K.M., Movellan, A., Aze, T., Dowsett, H. J., Giles Miller, C., Rios, N., and Hull, P. M., 2019, Endless Forams: >34,000 modern planktonic foraminiferal images for taxonomic training and automated species recognition using convolutional neural networks: Paleoceanography and Paleoclimatology, 34, 1157-1177. doi:10.1029/2019PA003612.

Itaki, T., Taira, Y., Kuwamori, N., Saito, H., Ikehara, M., and Hoshino, T., 2020, Innovative microfossil (radiolarian) analysis using a system for automated image collection and AI-based classification of species: Scientific Reports. doi:10.1038/s41598-020-77812-6.

Lever, J., Krzywinski, M., and Altman, N., 2017, Principal component analysis: Nature Methods, v. 14, p. 641–642.

Maass, W., 1997, Networks of spiking neurons: The third generation of neural network models: Neural Networks, v. 10, p. 1659–1671.

Marchant, R., Tetard, M., Pratiwi, A., Adebayo, M., and de Garidel-Thoron, T., 2020, Automated analysis of foraminifera fossil records by image classification using a convolutional neural network: Journal of Micropalaeontology, v. 39, p. 183–202.

686 Masquelier, T., and Thorpe, S.J., 2007, Unsupervised Learning of Visual Features through
687 Spike Timing Dependent Plasticity: PLOS Computational Biology, v. 3, p. e31.
688 Meunier, M., and Danelian, T., 2022, Astronomical calibration of late middle Eocene
689 radiolarian bioevents from ODP Site 1260 (equatorial Atlantic, Leg 207) and
690 refinement of the global tropical radiolarian biozonation: Journal of
691 Micropalaeontology, v. 41, p. 1–27.
692 Meunier, M., and Danelian, T., 2023, Progress in understanding middle Eocene nassellarian
693 (Radiolaria, Polycystinea) diversity; new insights from the western equatorial Atlantic
694 Ocean: Journal of Paleontology, v. 97, p. 1–25.
695 Mitra, R., Marchitto, T.M., Ge, Q., Zhong, B., Kanakiya, B., Cook, M.S., Fehrenbacher, J.S.,
696 Ortiz, J.D., Tripati, A., and Lobaton, E., 2019, Automated species-level identification
697 of planktic foraminifera using convolutional neural networks, with comparison to
698 human performance: Marine Micropaleontology, v. 148, p. 1-14.
699 doi:10.1016/j.marmicro.2019.01.005.
700 Moore, T.C., 1972, Mid-Tertiary Evolution of the Radiolarian Genus Calocycletta:
701 Micropaleontology, v. 18, p. 144–152.
702 Nigrini, C.A., Sanfilippo, A., and Moore, T.J., 2005, Radiolarian biostratigraphy and
703 chronology of radiolarian events of ODP Leg 199 sites and EW9709 sediment cores:
704 Supplement to: Nigrini, CA et al. (2005): Cenozoic Radiolarian Biostratigraphy: A
705 Magnetobiostratigraphic Chronology of Cenozoic Sequences from ODP Sites 1218,
706 1219, and 1220, Equatorial Pacific. In: Wilson, PA; Lyle, M; Firth, JV (Eds.)
707 Proceedings of the Ocean Drilling Program, Scientific Results, College Station, TX
708 (Ocean Drilling Program), v. 199, p. 1-76,
709 Https://Doi.Org/10.2973/Odp.Proc.Sr.199.225.2005,.

Obut, O., and Iwata, K., 2000, Lower Cambrian Rardiolaria from the Gorny Altai (southern West Siberia): Journal of Geology and Geophysics, v. 41.

Oksanen, J., Blanchet, F.G., Kindt, R., Legendre, P., Minchin, P.R., O'hara, R.B., Simpson, G.L., Solymos, P., Stevenes, M.H.H., Wagner, H., 2013, Package 'vegan': Community ecology package, v. 2, p. 1–295.

Paszke, A., Gross, S., Massa, F., Lerer, A., Bradbury, J., Chanan, G., Killeen, T., Lin, Z., Gimelshein, N., Antiga, L., Desmaison, A., Kopf, A., Yang, E., DeVito, Z., Raison, M., Tejani, A., Chilamkurthy, S., Steiner, B., Fang, L., Bai, J., and Chintala, S., 2019, PyTorch: An Imperative Style, High-Performance Deep Learning Library: 33rd NeurIPS, Vancouver, British Columbia, Canada, https://arxiv.org/abs/1912.01703

Pehle, C.-G., and Pedersen, J.E., 2021, Norse - A deep learning library for spiking neural networks (0.0.5), Zenodo, https://doi.org/10.5281/zenodo.4422025.

Pinto, F., Carlsson, V., Meunier, M., Van Bocxlaer., B., Elbez, H., Cueille, M., Boulet, P and Danelian, T, 2023, Data for the: Morphometrics and machine learning discrimination of the middle Eocene radiolarian species *Podocyrtis chalara*, *P. goetheana* and their morphological intermediates, Recherche Data Gouv, https://doi.org/10.57745/8KBOFP.

Pouille, L., Obut, O., Danelian, T., and Sennikov, N., 2011, Lower Cambrian (Botomian) polycystine Radiolaria from the Altai Mountains (southern Siberia, Russia): Comptes Rendus Palevol, v. 10, p. 627–633.

R Core Team, 2022, R: a language and environment for statistical computing: R Foundation for Statistical Computing. https://www.R-project.org.

Renaudie, J., Danelian, T., Saint Martin, S., Le Callonnec, L., and Tribovillard, N., 2010, Siliceous phytoplankton response to a Middle Eocene warming event recorded in the

734 tropical Atlantic (Demerara Rise, ODP Site 1260A): Palaeogeography,
735 Palaeoclimatology, Palaeoecology, v. 286, p. 121–134.
736 Renaudie, J., Lazarus, D., 2013, On the accuracy of paleodiversity reconstructions: a case
737 study in Antarctic Neogene radiolarians: Paleobiology, v. 39(3), p. 491-509.
738 Renaudie, J., Gray, R., and Lazarus, D.B., 2018, Accuracy of a neural net classification of
739 closely-related species of microfossils from a sparse dataset of unedited images. PeerJ
740 Preprints, 6:e27328v1.
741 Riedel, R.W., 1971, Cenozoic Radiolaria from the western tropical Pacific, Leg 7.: Init. Repts.
742 DSDP, v. 7, p. 1592–1627.
743 Riedel, W.R., and Sanfilippo, A., 1978, Stratigraphy and Evolution of Tropical Cenozoic
744 Radiolarians: Micropaleontology, v. 24, p. 61–96.
745 Ripley, B., Venables, B., Bates, D.M., Hornik, K., Gebhardt, A., Firth, D., Ripley, M.B.,
746 2013, Package 'mass': Cran r, 538, p. 113–120.
747 Rohlf, F., and Bookstein, F., 1991, Size and Shape (Book Reviews: Proceedings of the
748 Michigan Morphometrics Workshop.): Science, v. 253, p. 345-362.
749 Sanfilippo, A., and Riedel, W.R., 1970, Post-Eocene "Closed" Theoperid Radiolarians:
750 Micropaleontology, v. 16, p. 446–462.
751 Sanfilippo, A., and Riedel, W.R., 1992, The Origin and Evolution of Pterocorythidae
752 (Radiolaria): A Cenozoic Phylogenetic Study: Micropaleontology, v. 38, p. 1.
753 Sanfilippo, A., and Nigrini, C., 1998, Code numbers for Cenozoic low latitude radiolarian
754 biostratigraphic zones and GPTS conversion tables: Marine Micropaleontology, v. 33,
755 p. 109–156.
756 Schneider, C.A., Rasband, W.S., and Eliceiri, K.W., 2012, NIH Image to ImageJ: 25 years of
757 image analysis: Nature Methods, v. 9, p. 671–675.

Simonyan, K., and Zisserman, A., 2015, Very Deep Convolutional Networks for Large-Scale Image Recognition: ICLR, San Diego, California, USA, https://arxiv.org/abs/1409.1556.

Tavanaei, A., Ghodrati, M., Kheradpisheh, S. R., Masquelier, T., & Maida, A., 2019, Deep learning in spiking neural networks, Neural Networks, v. 111, p. 47-63, doi:10.1016/j.neunet.2018.12.002.

Tetard, M., Monnet, C., Noble, P., and Danelian T., 2017, Biodiversity patterns of Silurian Radiolaria: Earth-Science Reviews, v.173, p. 77-83.

Tetard, M., Marchant, R., Cortese, G., Gally, Y., de Garidel-Thoron, T., and Beaufort, L., 2020, Technical note: A new automated radiolarian image acquisition, stacking, processing, segmentation and identification workflow: Climate of the Past, v. 16, p. 2415–2429.

Venables, W.N., and Ripley, B.D., 2002, Random and Mixed Effects, *in* Venables, W.N. and Ripley, B.D., eds., Modern Applied Statistics with S, Statistics and Computing: New York, NY, Springer, p. 271–300.

Watanabe, M., Kawagata, S., Aita, Y., Suzuki, N., and Kamikuri, S., 2022, Changes in morphological parameters of the radiolarian Lampterium lineage from the middle Eocene in the tropical Pacific: Marine Micropaleontology, v. 173, 102125.

Westerhold, T., and Röhl, U., 2013, Orbital pacing of Eocene climate during the Middle Eocene Climate Optimum and the chron C19r event: Missing link found in the tropical western Atlantic: Orbital Pacing of Eocene Climate: Geochemistry, Geophysics, Geosystems, v. 14, p. 4811–4825.

Yang, Z.R., and Yang, Z., 2014, Artificial Neural Networks, Comprehensive Biomedical Physics: Elsevier, p. 1–17.

782 Zenke, F., and Ganguli, S., 2018, SuperSpike: Supervised Learning in Multilayer Spiking
783 Neural Networks: Neural Computation, v. 30, p. 1514–1541